# Uniaxial 2D Superlattice of Fe4 Molecular Magnets on Graphene

Luca Gragnaniello,*,[†] Fabian Paschke,[†] Philipp Erler,[†] Peter Schmitt,[‡] Nicole Barth,[†] Sabina Simon,[†] Harald Brune,[§] Stefano Rusponi,[§] and Mikhail Fonin*,[†]

[†]Department of Physics and [‡]Department of Chemistry, University of Konstanz, 78457 Konstanz, Germany
[§]Institute of Physics, École Polytechnique Fédérale de Lausanne (EPFL), Station 3, CH-1015 Lausanne, Switzerland

ABSTRACT: We demonstrate that electrospray deposition enables the fabrication of highly periodic self-assembled arrays of Fe_4H single molecule magnets on graphene/Ir(111). The energetic positions of molecular states are probed by means of scanning tunneling spectroscopy, showing pronounced long- and short-ranged spatial modulations, indicating the presence of both locally varying intermolecular as well as adsorption-site dependent molecule–substrate interactions. From the magnetic field dependence of the X-ray magnetic circular dichroism signal, we infer that the magnetic easy axis of each Fe_4H molecule is oriented perpendicular to the sample surface and that after the deposition the value of the uniaxial anisotropy is identical to the one in bulk. Our findings therefore suggest that the observed interaction of the molecules with their surrounding does not modify the molecular magnetism, resulting in a two-dimensional array of molecular magnets that retain their bulk magnetic properties.

KEYWORDS: *Single-molecule magnet, graphene, scanning tunneling microscopy, scanning tunneling spectroscopy, X-ray magnetic circular dichroism, electrospray deposition*
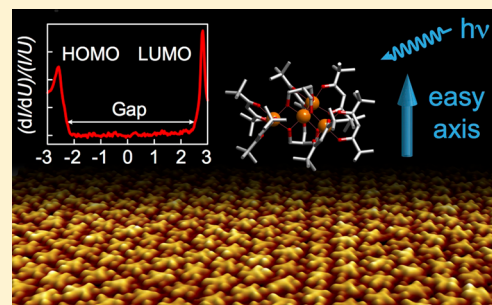
For decades, single-molecule magnets (SMMs) were attractive candidates as building blocks for new technologies such as spintronics and molecular electronics.[1,2] For possible applications, it is crucial to be able to bring the molecules at surfaces and to preserve their magnetic properties despite the interactions with the substrate.[3−6] At the same time, it is highly desirable to be able to arrange SMMs in ordered networks, which are usually found for simple-structured planar molecules, like phthalocyanines,[7−9] but can be hard to achieve for more complex polynuclear compounds.

Among the latter, the tetranuclear iron(III) cluster $[Fe_4(L)_2(dpm)_6]$ (with H_3L being of the general form R-$C(CH_2OH)_3$ and Hdpm = dipivaloylmethane), commonly named Fe_4, is known to combine peculiar magnetic properties with a superior chemical stability.[10,11] Indeed, it was recently shown that Fe_4 SMMs provide a paradigmatic system for the study of substrate effects on the quantum dynamics of magnetic properties when deposited on graphene, with potential applications in spin-nanomechanical and nanospintronic devices.[12] However, thermal deposition of Fe_4 is hampered by the fragmentation of the compound,[13] and neither long-range ordered self-assembly nor a uniform orientation of the easy magnetization axis of Fe_4 is observed for the protruding tripodal ligands L that are typically used to graft the molecules to the substrate.[10−12,14−16] Nevertheless, we were recently able to overcome this limit by employing electrospray deposition (ESD)[17−20] and using a suitable Fe_4 derivative, namely Fe_4H, which was specifically tailored with the shortest tripodal ligand possible (R = H, see Figure 1a).[21]

In this work, we demonstrate that by using ESD as a deposition method and graphene/Ir(111) as a substrate, it is possible to organize the Fe_4H SMMs in highly ordered two-dimensional assemblies with a well-defined adsorption geometry. Molecular states are probed by means of scanning tunneling spectroscopy (STS), showing spatial variations in energy due to intermolecular and molecule–substrate interactions. Magnetization curves obtained on an Fe_4H sub-monolayer by means of X-ray magnetic circular dichroism (XMCD) provide direct access to the magnetic properties of the Fe_4H complex on the substrate, indicating uniaxial out-of-plane orientation of the magnetic easy axis and a magnetic anisotropy identical to that in bulk. As a result, we find that the bistable magnetic behavior of Fe_4H is fully preserved in the 2D superlattice on the graphene surface in spite of the observed interaction with the surrounding.

Typical scanning tunneling microscopy (STM) images of the Fe_4H/graphene/Ir(111) system at a submonolayer coverage are shown in Figure 1b−d. The molecules are found to arrange in two-dimensional islands with an apparent height of around 750 pm, which are often adjacent to the monatomic step-edges of the graphene/Ir(111) substrate (Figure 1b). High-resolution images reveal a clear intramolecular structure that comprises six protrusions and an almost three-fold rotational symmetry (Figure 1c,d). The intramolecular structure is identical to that already reported for Fe_4H on h-BN/Rh(111),[21] showing that Fe_4H adsorbs on the graphene layer in the same flat geometry with the four Fe atoms arranged in a plane parallel to the
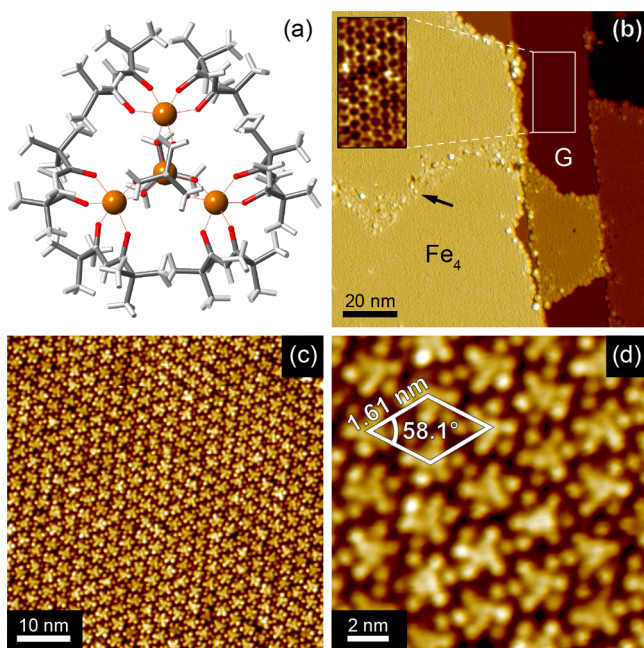
Figure 1. (a) Structure of the Fe_4H compound viewed along the [001] lattice direction of the molecular crystal. Color code: Fe = orange, O = red, C = gray, H = white. (b−d) STM topographic images (U = +3 V, I = 10 pA, T = 1.9 K) of Fe_4H molecules on graphene/Ir(111) at different magnifications. The inset in panel b highlights the graphene moiré structure that is apparent within the substrate regions that are not covered by molecules. The arrow marks a domain wall that forms the border between two presumably separately grown Fe_4H islands. The unit cell of the molecular superlattice is highlighted in panel d.

Figure 2. (a) Typical tunneling spectra (U_{set} = +3 V, I_{set} = 15 pA, T = 1.9 K) obtained on the dpm ligands (red) and on the center (black) of an individual Fe_4H molecule, as well as on the clean substrate next to the molecule (gray). (b) STM topography image (1.6 × 1.6 nm², U = +3 V, I = 15 pA, T = 1.9 K) of the Fe_4H molecule measured in panel a together with the corresponding conductance maps obtained at different bias voltages. The scale bar reflects the magnitude of the (dI/dU)/(I/U) signal. (c−e) Histograms showing the distribution of STS peak positions as obtained from measurements on a large number of molecules, as well as the distribution of the energy gaps corresponding to the distance between the peak maxima. Solid curves are Gaussian fits to the histograms highlighting the mean values and standard deviations.

sample surface. Consequently, the six protrusions are identified as the six dpm ligands of the molecule.

The arrangement of the molecules within the islands is highly periodic with an intermolecular distance of (1.61 ± 0.10)nm and an intermolecule angle of (58.1 ± 1.8)° (Figure 1d). These lattice parameters are close to the intrinsic ordering in Fe_4H single crystals, in which intermolecular distances and angles within the crystallographic (001) plane are in the range of 1.622−1.632 nm and 59.8°−60.4°, respectively.[21] In contrast to the Fe_4H/*h*-BN/Rh(111) system, no correlation is observed for Fe_4H/graphene/Ir(111) between the molecular assembly and the moiré superstructure of the substrate, which can be resolved on the uncovered graphene/Ir(111) areas next to the Fe_4H islands (Figure 1b inset). Furthermore, no isolated Fe_4H molecules are found on the surface. These observations demonstrate a rather weak impact of the graphene/Ir(111) substrate on the lateral adsorption sites, similar to the behavior observed for Er(trensal) SMMs on the same substrate.[22]

To gain insight into the electronic properties of Fe_4H SMMs on graphene/Ir(111), we performed differential conductance (dI/dU) measurements both at the center of the molecules and at the dpm ligands. To ensure integrity of the molecules during acquisition, low stabilization currents of I_{set} = 10−20 pA at a bias voltage of U_{set} = +3 V are required. Typical spectra obtained on an individual molecule are shown in Figure 2a. The spectra are characterized by two peaks, occurring on average at −(2.64 ± 0.22) eV and +(2.77 ± 0.22) eV when the tip is positioned above the center of the molecule, whereas a small shift of the peaks to −(2.76 ± 0.16) eV and +(2.67 ± 0.13) eV is observed when measured at the dpm ligands. The average

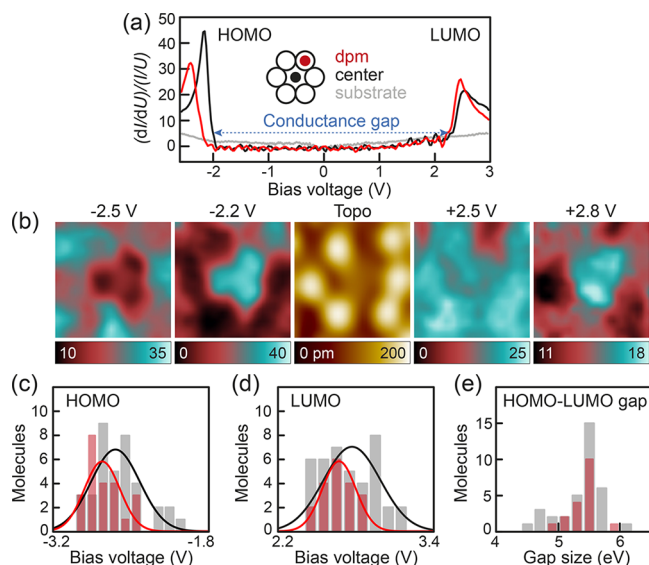line width of the peaks is (410 ± 180) meV for both positive and negative resonances.

We assign resonances measured at positive and negative bias voltage to elastic tunneling into the lowest unoccupied and the highest occupied molecular orbitals (LUMO and HOMO) of Fe_4H, respectively. To support this assumption, we acquired conductance maps on a single Fe_4H molecule, shown in Figure 2b. The bias voltages of the presented maps roughly correspond to the resonance energies visible in the spectra shown in Figure 2a. For large negative bias of −2.5 V, the measured intensity is spread over the outer ligand shell of the Fe_4H molecule. At the bias voltage of −2.2 V, we observe a localization of the orbital intensity distribution toward the center of the Fe_4H molecule yielding a feature of the three-fold symmetry with spectral weight spread toward three of the six dpm ligands. At lower positive bias of +2.5 V, the spectral intensity is homogeneously distributed over the whole molecule reproducing the shape of the Fe_4H molecule constituted by the inner core and six outer dpm ligands. Increasing the bias voltage to +2.8 V leads to an intensity redistribution with the central part gaining substantial spectral weight, which constitutes a feature with three-fold symmetry connected to three dpm ligands. The overall appearance of a Fe_4H molecule undergoes substantial changes upon going from negative to positive bias voltages and thus stems from different molecular orbitals. Compared to the density functional theory (DFT) calculations carried out for an isolated Fe_4H molecule,[21] we find a good agreement with our experimental findings with the orbital states of the LUMO being localized over the outer and inner Fe atoms, respectively. Concerning the HOMO,
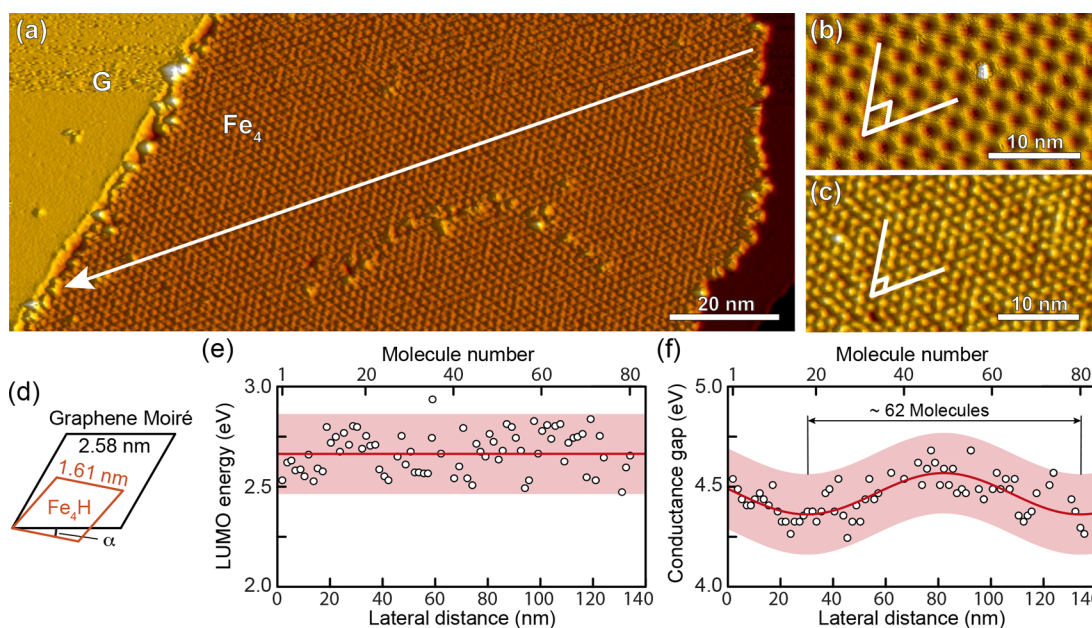
Figure 3. Spatial modulation of the HOMO and LUMO energies. (a) STM topography of an Fe₄H island on graphene/Ir(111) (U = +3 V, I = 20 pA, T = 1.8 K). (b) Close-up view of the graphene/Ir(111) moiré structure directly to the right of the island (U = +100 mV, I = 1 nA). (c) Close-up view of the Fe₄H island. (d) Model of the two unit cells. α denotes the rotational angle, not to scale. (e) Spatial variation of the LUMO peak energy, as obtained from STS spectra taken on the center of different Fe₄H molecules along the white arrow in panel a. The mean value is shown as a red line, together with an energy band of ± 0.2 eV as a guide to the eye. (f) Spatial variation of the conductance gap for the same sequence of molecules. Note that the conductance gap instead of the HOMO−LUMO gap (cf. Figure 2a) is given here since negative bias voltage values were limited to −2.5 V for stability reasons. A sine-fit to the data (red line) is shown, together with an energy band of the same width as in panel e.

calculations show molecular states being spread over dpm and tripodal ligands, which is in accordance with the measurements except for the absolute energetic positions.

Figure 2c−e show histograms of the peak positions and of the energy gap between both peaks measured on a large number of molecules. The average HOMO−LUMO gap is (5.4 ± 0.3) eV for both the center and dpm ligand measurement positions, being larger than the 3.9 eV predicted for an isolated Fe₄H molecule. We attribute this discrepancy to the typical underestimation of band gap values by DFT in organic materials. The scattering in the HOMO and LUMO peak energies and in the HOMO−LUMO gap values for different molecules visible in Figure 2c−e points to the presence of locally varying intermolecular or molecule−substrate interactions. While local variations in intermolecular interactions caused by imperfections in the periodic molecular assembly are expected to appear in a chaotic spatial pattern, the impact of molecule−substrate interactions should result in a long-range modulation, according to the position of the molecules with respect to the graphene moiré pattern. Two different mechanisms resulting in a shift of the molecular energy levels due to molecule−substrate interactions are conceivable. On the one hand, a local work function variation on the order of 0.1 eV[23] across the graphene moiré unit cell is generally expected to uniformly shift both the HOMO and LUMO peak energies for different adsorption sites, therefore keeping the energy gap unaffected. On the other hand, different adsorption sites within the moiré unit cell might result in different molecule−substrate coupling strengths,[8] potentially leading to unequal shifts of the HOMO and LUMO peak energies and therefore to an alteration of the energy gap.

To determine the prominent coupling mechanism, we have taken STS spectra for a sequence of neighboring molecules in a homogeneously ordered Fe₄H domain, shown in Figure 3a. For

this specific Fe₄H domain, the unit cell of the molecular assembly is found to be rotated by an angle of α = 1.3 ± 0.5° with respect to the unit cell of the graphene moiré pattern, resulting in a distance of 99 nm or roughly 61 molecules between two virtually identical adsorption sites (Figure 3b−d).

The variations of the LUMO peak energy and of the conductance gap measured along the sequence of molecules are plotted in Figure 3e and 3f, respectively. While short-range correlations of the LUMO peak energies can be identified in Figure 3e, our data show no clear long-range correlation of the LUMO peak energy on the length-scale of adsorption site variations. The observed scattering in the LUMO peak energy is therefore likely dominated by varying molecule−molecule interactions. Notably, the impact of local work function variations across the graphene moiré unit cell on the LUMO peak energy is apparently too small to be directly observed in our measurement.

In contrast, the conductance gap variation shown in Figure 3f clearly shows a long-range correlation. A fit of a sine-function to our data results in a modulation amplitude of ∼100 meV and a period of ∼62 molecules. This perfectly matches the expected scale of adsorption site variations and therefore shows the influence of molecule−substrate interactions on the electronic states of Fe₄H. A similar effect was reported for CoPc molecules on Gr/SiO₂ and on h-BN.[8] We note that the observed variation in the conductance gap might be caused by both a shift of the HOMO and LUMO peak energies and a change of the HOMO and LUMO line widths.

Considering the observed impact of intermolecular and molecule−substrate interactions, the question arises whether the magnetic bulk properties of Fe₄H are preserved when placed on graphene/Ir(111). We therefore employed X-ray absorption spectroscopy (XAS) and XMCD measurements to further investigate the electronic structure and to address the

magnetic properties of the surface-supported Fe_4H molecules. Both methods provide highly surface sensitive and element selective information about oxidation states and magnetic moments and are therefore considered to be key tools for studying electronic and magnetic phenomena at surfaces. Figure 4a shows XAS and XMCD spectra recorded at the Fe $L_{2,3}$ ($2p \rightarrow 3d$) absorption edges for a sample with 0.55 monolayer (ML) Fe_4H on graphene/Ir(111), at normal incidence.
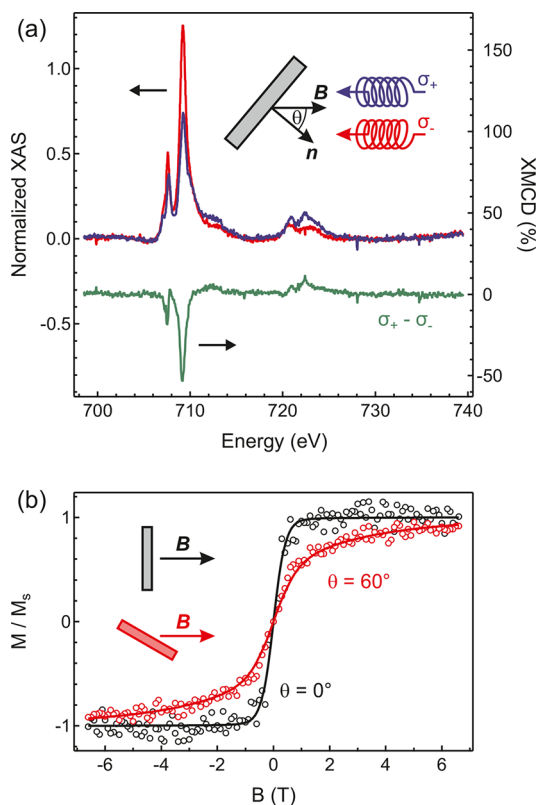

Figure 4. (a) XAS (blue/red) and XMCD (green) spectra at the Fe $L_{2,3}$ edges, obtained on 0.55 ML Fe_4H on graphene/Ir(111). The spectra were acquired at normal incidence in a magnetic field of 6.8 T and at $T \simeq 3$ K. σ_+ and σ_- refer to left and right polarized light, respectively. All spectra are normalized to the value of $(\sigma_+ + \sigma_-)/2$ at the peak of the L_3 edge (709.2 eV). (b) Symmetrized magnetization curves obtained by recording the magnetic field dependence of the XMCD signal at 709.2 eV for the same sample. Solid lines represent fits to the data based on the model described in the text.

The spectral features observed in XAS are in very good agreement with data reported for similar Fe_4 derivatives.[10,11,15,24−27] This also applies to the shape and magnitude of the XMCD signal, which have been associated with a ferrimagnetic arrangement of the four Fe^{3+} spins,[25] thus suggesting that the molecules retain their $S = 5$ spin ground state on the graphene surface. To investigate this aspect, we employed sum rules,[28,29] assuming five holes of $3d$ levels per Fe atom. For the orbital magnetic moment, we find a value of $m_L = (0.13 \pm 0.07)$ μ_B/atom. The presence of a non-negligible, albeit small, orbital magnetic moment is in seeming contradiction to the literature on Fe_4 SMMs, in which the magnetic moment has been generally assumed to be of pure spin origin.[30] However, it is clear that a small orbital magnetic moment must be present,

as the magnetic anisotropy of Fe_4 originates from spin−orbit interaction.[31]

To determine the value of the effective spin magnetic moment per Fe atom $2 \langle S_z \rangle + 7 \langle D_z \rangle$, we further employ the XMCD spin sum rule. In case of Fe^{3+}, the magnetic dipole operator $\langle D_z \rangle$ is zero, because the $3d$ shell is half-filled. Therefore, the effective spin moment equals the spin moment $\langle S_z \rangle$. However, the accuracy of the spin sum rule for $3d^5$ metal systems is restricted due to the mixing and overlap of the L_3 and L_2 edges, resulting in a general underestimation of the spin moment of the order ∼30%.[32] Here, we obtain a value of $m_S = (1.85 \pm 0.1)$ μ_B/atom. Considering the systematic underestimation, this value is consistent with an expected mean spin moment of 2.5 μ_B/atom due to the ferrimagnetic alignment of the four Fe^{3+} spins.

Magnetization curves of the Fe_4H submonolayer were obtained by measuring the magnetic field dependence of the XMCD signal at the peak of the L_3 edge (709.2 eV). Figure 4b shows data recorded at normal ($\theta = 0°$) and grazing ($\theta = 60°$) incidences. While the shape of the XAS and XMCD spectra remained unchanged within the accuracy of our measurement on the time scale of acquiring individual spectra, we observed a small decrease in the XMCD amplitude at the L_3 edge of the order of a few percent after several hours of X-ray beam exposure, indicating that minimum radiation damage was occurring while recording magnetization curves. This resulted in a slight error in the experimental data, which is corrected here to first order by symmetrizing the curves, that is, replacing $M(H)$ with $[M(H) - M(-H)]/2$.

The striking feature of the data presented in Figure 4b is that the magnetization obtained at normal incidence is significantly steeper than at grazing incidence, indicating an out-of-plane magnetic anisotropy of the sample. Since the easy magnetization axis of Fe_4 is oriented perpendicular to the plane of the four Fe atoms,[11,15,31] this result is in perfect agreement with the planar adsorption geometry observed in STM topography.

To quantitatively analyze the recorded magnetization curves, we perform a fit to the experimental data using a simple spin Hamiltonian $\mathcal{H}_{ZFS} = DS_z^2 + g\mu_B\mathbf{S}\cdot\mathbf{H}$, where S_z is the out-of-plane component of the total spin $\mathbf{S}$, D is the anisotropy constant, g the Landé factor, and $\mathbf{H}$ the external magnetic field. The fitting of the data was carried out by keeping the spin quantum number and Landé factor fixed to $S = 5$ and $g = 2$, respectively, and refining the temperature T and anisotropy constant D. A possible slight deviation of the Landé factor from $g = 2$ due to a small orbital contribution to the magnetic moment is not considered here, as it is not expected to significantly affect our analysis. The best-fit parameters so obtained are $T = (2.8 \pm 0.3)$ K and $D = -(64 \pm 8)$ μeV. Calculated magnetization curves corresponding to the best-fit result are plotted as solid lines in Figure 4b and are in excellent agreement with our experimental data. This justifies our assumptions of an out-of-plane orientation of the magnetic easy axis and of an $S = 5$ spin ground state of Fe_4H on graphene/Ir(111). We note that the anisotropy constant D of the Fe_4H submonolayer coincides within the accuracy of our measurement with that of Fe_4H bulk material, as obtained from superconducting quantum interference device (SQUID) magnetometry on polycrystalline powder.[21] We therefore conclude that the magnetic anisotropy constant of Fe_4H SMMs is entirely preserved upon the deposition on graphene/Ir(111).

In summary, by using a combination of microscopic and spectroscopic techniques, we show that a highly periodic self-assembly of Fe_4H molecules can be realized on graphene/Ir(111) with lattice parameters of the molecular supercell close to those found in Fe_4H bulk material. According to high resolution STM images, the molecules adsorb in a planar geometry with the four Fe atoms being located in a plane parallel to the sample surface. This finding is corroborated by XMCD measurements performed at different orientations of the magnetic field, showing that the magnetic easy axis of the molecules is oriented perpendicular to the sample surface. From a quantitative analysis of the magnetic field dependence of the XMCD spectra, we find that the uniaxial anisotropy constant of Fe_4H is unaffected upon the deposition on graphene/Ir(111). This finding is remarkable with regard to our STS measurements, which reveal local variations in intermolecular and molecule–substrate interactions on the order of 200 meV, demonstrating the robustness of the molecular magnetism of the Fe_4 complex. Our findings identify Fe_4H on graphene/Ir(111) as a very attractive system for investigation of further magnetic and electronic effects, like quantum tunneling of magnetization or adsorption site specific inelastic tunneling measurements to determine the nearest-neighbor magnetic exchange energy J_1.

Methods. Scanning tunneling microscopy and spectroscopy experiments were performed in a two-chamber ultra-high vacuum (UHV) system (base pressure 5×10^{-11} mbar), equipped with an Omicron Cryogenic-STM. The STM was operated at temperatures of 1.8–8 K. All STM measurements were carried out in the constant-current mode using grinded and polished PtIr tips (Nanoscore GmbH). Positive bias voltage (U) corresponds to probing unoccupied states of the sample. Differential conductance spectra were recorded by modulating the gap voltage (f_{mod} = 692 Hz, V_{mod} = 40 mV rms) and using standard lock-in detection. For conductance maps, $I(U)$ spectra were collected on a 30×30 grid over an area of 1.6×1.6 nm^2. The obtained spectra were numerically differentiated and normalized to the I/U signal. Spatial maps at specific bias voltages were derived from the spectroscopy data.

X-ray absorption spectroscopy and X-ray magnetic circular dichroism experiments were performed at the X-Treme beamline[33] of the Swiss Light Source at the Paul Scherrer Institut. The XAS and XMCD measurements were performed in the total electron yield mode, with the X-ray beam and magnetic field being aligned parallel to each other and forming an angle θ with the surface normal.

Samples were prepared *in situ* for all experiments presented. The Ir(111) single crystal (Surface Preparation Laboratory B. V.) was cleaned by repeated cycles of Ar^+ sputtering at 2 kV, heated in an O_2 atmosphere of 5×10^{-7} mbar at 900–1150 °C, and flash annealed in UHV up to 1150 °C. Graphene was prepared by exposing the clean Ir(111) surface to an ethylene partial pressure of 1×10^{-7} mbar for 20 min while keeping the sample at T = 1100 °C. A good quality of the graphene layers was verified by means of STM imaging. Electrospray deposition of Fe_4H was performed as described elsewhere.[21] The surface coverage was estimated by correlating XAS and STM data obtained at the synchrotron.

■ AUTHOR INFORMATION

Corresponding Authors
*E-mail: luca.gragnaniello@uni-konstanz.de.
*E-mail: mikhail.fonin@uni-konstanz.de.
ORCID ⊙
Luca Gragnaniello: 0000-0003-1150-3941
Harald Brune: 0000-0003-4459-3111
Stefano Rusponi: 0000-0002-8494-5532

Notes
The authors declare no competing financial interest.

■ REFERENCES

(1) Bogani, L.; Wernsdorfer, W. *Nat. Mater.* **2008**, *7*, 179−186.
(2) Gruber, M.; Ibrahim, F.; Boukari, S.; Isshiki, H.; Joly, L.; Peter, M.; Studniarek, M.; Da Costa, V.; Jabbar, H.; Davesne, V.; et al. *Nat. Mater.* **2015**, *14*, 981−984.
(3) Bogani, L.; Cavigli, L.; Gurioli, M.; Novak, R. L.; Mannini, M.; Caneschi, A.; Pineider, F.; Sessoli, R.; Clemente-Leon, M.; Coronado, E.; et al. *Adv. Mater.* **2007**, *19*, 3906−3911.
(4) Salman, Z.; Chow, K. H.; Miller, R. I.; Morello, A.; Parolin, T. J.; Hossain, M. D.; Keeler, T. A.; Levy, C. D. P.; MacFarlane, W. A.; Morris, G. D.; et al. *Nano Lett.* **2007**, *7*, 1551−1555.
(5) Moro, F.; Biagi, R.; Corradini, V.; Evangelisti, M.; Gambardella, A.; De Renzi, V.; del Pennino, U.; Coronado, E.; Forment-Aliaga, A.; Romero, F. M. *J. Phys. Chem. C* **2012**, *116*, 14936−14942.
(6) Wäckerlin, C.; Donati, F.; Singha, A.; Baltic, R.; Rusponi, S.; Diller, K.; Patthey, F.; Pivetta, M.; Lan, Y.; Klyatskaya, S.; et al. *Adv. Mater.* **2016**, *28*, 5195−5199.
(7) Hämäläinen, S. K.; Stepanova, M.; Drost, R.; Liljeroth, P.; Lahtinen, J.; Sainio, J. *J. Phys. Chem. C* **2012**, *116*, 20433−20437.
(8) Järvinen, P.; Hämäläinen, S. K.; Banerjee, K.; Häkkinen, P.; Ijäs, M.; Harju, A.; Liljeroth, P. *Nano Lett.* **2013**, *13*, 3199−3204.
(9) Bazarnik, M.; Brede, J.; Decker, R.; Wiesendanger, R. *ACS Nano* **2013**, *7*, 11341−11349.
(10) Mannini, M.; Pineider, F.; Sainctavit, P.; Danieli, C.; Otero, E.; Sciancalepore, C.; Talarico, A. M.; Arrio, M.-A.; Cornia, A.; Gatteschi, D.; et al. *Nat. Mater.* **2009**, *8*, 194−197.
(11) Mannini, M.; Pineider, F.; Danieli, C.; Totti, F.; Sorace, L.; Sainctavit, P.; Arrio, M.-A.; Otero, E.; Joly, L.; Cezar, J. C.; et al. *Nature* **2010**, *468*, 417−421.
(12) Cervetti, C.; Rettori, A.; Pini, M. G.; Cornia, A.; Repollés, A.; Luis, F.; Dressel, M.; Rauschenbach, S.; Kern, K.; Burghard, M.; et al. *Nat. Mater.* **2015**, *15*, 164−168.
(13) Lanzilotto, V.; Malavolti, L.; Ninova, S.; Cimatti, I.; Poggini, L.; Cortigiani, B.; Mannini, M.; Totti, F.; Cornia, A.; Sessoli, R. *Chem. Mater.* **2016**, *28*, 7693−7702.
(14) Margheriti, L.; Mannini, M.; Sorace, L.; Gorini, L.; Gatteschi, D.; Caneschi, A.; Chiappe, D.; Moroni, R.; de Mongeot, F. B.; Cornia, A.; et al. *Small* **2009**, *5*, 1460−1466.
(15) Malavolti, L.; Lanzilotto, V.; Ninova, S.; Poggini, L.; Cimatti, I.; Cortigiani, B.; Margheriti, L.; Chiappe, D.; Otero, E.; Sainctavit, P.; et al. *Nano Lett.* **2015**, *15*, 535−541.
(16) Burgess, J. A.; Malavolti, L.; Lanzilotto, V.; Mannini, M.; Yan, S.; Ninova, S.; Totti, F.; Rolf-Pissarczyk, S.; Cornia, A.; Sessoli, R.; et al. *Nat. Commun.* **2015**, *6*, 8216.
(17) Saywell, A.; Magnano, G.; Satterley, C. J.; Perdigao, L. M. A.; Britton, A. J.; Taleb, N.; del Carmen Giménéz-López, M.; Champness, N. R.; O'Shea, J. N.; Beton, P. H. *Nat. Commun.* **2010**, *1*, 75.
(18) Rauschenbach, S.; Stadler, F. L.; Lunedei, E.; Malinowski, N.; Koltsov, S.; Costantini, G.; Kern, K. *Small* **2006**, *2*, 540−547.
(19) Rauschenbach, S.; Vogelgesang, R.; Malinowski, N.; Gerlach, J. W.; Benyoucef, M.; Costantini, G.; Deng, Z.; Thontasen, N.; Kern, K. *ACS Nano* **2009**, *3*, 2901−2910.

(20) Kahle, S.; Deng, Z.; Malinowski, N.; Tonnoir, C.; Forment-Aliaga, A.; Thontasen, N.; Rinke, G.; Le, D.; Turkowski, V.; Rahman, T. S.; et al. *Nano Lett.* **2012**, *12*, 518−521.

(21) Erler, P.; Schmitt, P.; Barth, N.; Irmler, A.; Bouvron, S.; Huhn, T.; Groth, U.; Pauly, F.; Gragnaniello, L.; Fonin, M. *Nano Lett.* **2015**, *15*, 4546−4552.

(22) Dreiser, J.; Pacchioni, G. E.; Donati, F.; Gragnaniello, L.; Cavallin, A.; Pedersen, K. S.; Bendix, J.; Delley, B.; Pivetta, M.; Rusponi, S.; et al. *ACS Nano* **2016**, *10*, 2887−2892.

(23) Altenburg, S. J.; Berndt, R. *New J. Phys.* **2014**, *16*, 053036.

(24) Mannini, M.; Pineider, F.; Sainctavit, P.; Joly, L.; Fraile-Rodríguez, A.; Arrio, M.-A.; Cartier dit Moulin, C.; Wernsdorfer, W.; Cornia, A.; Gatteschi, D.; et al. *Adv. Mater.* **2009**, *21*, 167−171.

(25) Mannini, M.; Tancini, E.; Sorace, L.; Sainctavit, P.; Arrio, M.-A.; Qian, Y.; Otero, E.; Chiappe, D.; Margheriti, L.; Cezar, J. C.; et al. *Inorg. Chem.* **2011**, *50*, 2911−2917.

(26) Rodriguez-Douton, M. J.; Mannini, M.; Armelao, L.; Barra, A.-L.; Tancini, E.; Sessoli, R.; Cornia, A. *Chem. Commun.* **2011**, *47*, 1467−1469.

(27) Perfetti, M.; Pineider, F.; Poggini, L.; Otero, E.; Mannini, M.; Sorace, L.; Sangregorio, C.; Cornia, A.; Sessoli, R. *Small* **2014**, *10*, 323−329.

(28) Thole, B. T.; Carra, P.; Sette, F.; van der Laan, G. *Phys. Rev. Lett.* **1992**, *68*, 1943−1946.

(29) Carra, P.; Thole, B. T.; Altarelli, M.; Wang, X. *Phys. Rev. Lett.* **1993**, *70*, 694−697.

(30) Accorsi, S.; Barra, A.-L.; Caneschi, A.; Chastanet, G.; Cornia, A.; Fabretti, A. C.; Gatteschi, D.; Mortalò, C.; Olivieri, E.; Parenti, F.; et al. *J. Am. Chem. Soc.* **2006**, *128*, 4742−4755.

(31) Ribas-Arino, J.; Baruah, T.; Pederson, M. R. *J. Chem. Phys.* **2005**, *123*, 044303.

(32) Piamonteze, C.; Miedema, P.; de Groot, F. M. F. *Phys. Rev. B: Condens. Matter Mater. Phys.* **2009**, *80*, 184410.

(33) Piamonteze, C.; Flechsig, U.; Rusponi, S.; Dreiser, J.; Heidler, J.; Schmidt, M.; Wetter, R.; Calvi, M.; Schmidt, T.; Pruchova, H.; et al. *J. Synchrotron Rad.* **2012**, *19*, 661−674.